UNIVERSIDAD DE CANTABRIA

Facultad de Ciencias

Departamento de Física Aplicada

Tesis Doctoral

SYNTHESIS, STRUCTURAL CHARACTERIZATION AND SPECTROSCOPIC STUDY OF NANOCRYSTALLINE AND MICROCRYSTALLINE MATERIALS

Rosa Martín Rodríguez

Santander, Noviembre de 2010

Chapter 2

Theory

2.1 Introduction

The models and approximations utilized for the interpretation of the experimental data are presented along this chapter. Firstly, the increasing interest of nanomaterials regarding both fundamental studies and applications is outlined. Secondly, the determination of the energy levels of an ion in a crystal, and the transitions among these levels, responsible for the RE and TM ions optical properties, are described. From Fermi's Golden Rule which defines the transition probability, concepts like the transition lifetime are introduced. Non-radiative relaxation processes, responsible for most of the luminescence quenching, and the different UC mechanisms, as well as the basic concepts of Raman spectroscopy are also explained. Moreover, the size dependence of the optical properties in semiconductor nanoparticles is deduced. Finally, structural phase transitions are briefly described.

2.2 Interest of nanoparticles

Remarkable examples of nanotechnology throughout history are the famous *Lycurgus Cup* which shows dichroism due to the interaction of light with metal nanoparticles embedded in a glass matrix, or the addition of metallic constituents to glass, in order to create stained glass windows [1]. Nowadays, nanoscience and nanotechnology deal with the study of materials with size in the nanometer range, which is extremely interesting for several reasons. Firstly, relevant physical laws change at the nanometric scale, this is, many of the classical laws are not valid anymore and quantum mechanics must be applied. Besides

quantum confinement effects [2], changes with size reduction are related to the higher surface-to-volume ratio in nanoparticles [3], [4]. Secondly, some metastable phases are only observed in reduced-size materials [5]. Thirdly, diverse areas of technology have pointed their attention in the last years to make smaller components not only for electronics but also in other fields like new materials, health-sciences or renewable energy sources [1], [6]. The well-known Moore's law summarizes the scale to get the same function by making the working elements smaller. The tunnel diode is the first example in which the appearance of quantum physics at small sizes led to a new device. The fact that the energy gap of QDs, and therefore the emitting wavelength, is blue-shifted when particle size decreases, is of great interest for solar cells and bio-labeling [7], [8]. Carbon black which contains carbon nanotubes, has been used for a long time as an additive to the rubber in automobile tires. Other examples in which the industry has taken advantage of nanomaterials are titanium dioxide pigment in white paint, large synthetic biomolecules or nanoparticle slurries for polishing.

Moving to our research field, there is a considerable interest in the development of highly-luminescent nanomaterials for biological applications such as bio-labeling, drug delivery or diagnostics. Metallic and magnetic nanoparticles with the adequate organic capping, and core-shell semiconductor nanocrystals, have been widely used in biological experiments [8], [9], [10]. Water-soluble nanocrystals as well as materials with appropriate optical properties are needed. In this sense, the study of the optical properties of RE-doped nanoparticles for biological applications is increasing because of lanthanides properties such as narrow absorption and emission bands, high quantum efficiency, and long lifetimes [11], [12], [13]. Different nanomaterials find also applications in renewable energy sources such as photovoltaic solar cells technology [7], [14]. UC and downconversion processes in nanoparticles doped with RE or TM ions may also be implemented for this purpose. For instance, $NaYF_4$: Er^{3+} phosphors have been proposed for the enhancement of solar cells response [15], [16].

2.3 Insulating materials. Optical properties

2.3.1 Doped insulators

Insulators tend to be colorless since they are characterized by a transparency range in the ultraviolet (UV)- visible - near infrared (NIR) range. The sharp drop in the transmission for $\lambda > 6000$ nm is caused by vibrational absorption, while in the UV spectral region, $\lambda <$ 200 nm, it is due to absorption in the material bandgap. Insulating hosts can present new optical properties thanks to the presence of dopant impurity ions, such as RE or TM ions [17]. The properties of the optically active ions may be understood according to the idea of a coordination complex, AB_n. It is a structure consisting of a central cation A bonded to the n closest neighbors B, called ligands.

2.3.2 Ions in a static crystalline environment

According to a point-charge model, the valence electrons belong to the dopant ion A, and the effect of the lattice modifies its energy levels by the influence of the ligand ions B through the electric field that they produce at the site of A. This electrostatic field is called the crystal-field, and the Hamiltonian can be written as [18], [19], [20]:

$$H = H_{FI} + H_{CF} \tag{2.1}$$

H_{FI} being the free ion A Hamiltonian, and H_{CF} the crystal-field Hamiltonian:

$$H_{FI} = H_0 + H' + H_{SO} \tag{2.2}$$

where H_0 includes the kinetic and potential energy in the central-field approximation, due to the nucleus and the inner closed-shell electrons, H' corresponds to the Coulomb interaction among the outer electrons, and H_{SO} describes the interaction between the magnetic moment of the electron, s, and its angular moment, l, and it is known as the spin-orbit coupling.

Depending on the relative importance of the different terms, diverse approaches can be considered in order to diagonalize the Hamiltonian:

- *Weak crystal field*: $H_{CF} \ll H_{SO}, H', H_0$. In this regime the energy levels of the free ion A are only slightly perturbed by the crystal field. H_{CF} is taken as a perturbation over the $^{2S+1}L_J$ states ($J = L+S$). It is appropriate to describe the energy levels of trivalent RE ions, since for these ions the optically active 4f electrons are screened by the outer filled $5s^2 5p^6$ sub-shells. These electrons partially shield the crystal field created by the B ions.

- *Intermediate crystal field*: $H_{SO} \ll H_{CF} < H'$. In this case the spin-orbit interaction which is weaker than the crystal field, is initially neglected. The crystal field is considered a perturbation on the ^{2S+1}L terms.

- *Strong crystal field*: $H_{SO} < H' < H_{CF}$. In this approach the crystal field term dominates over the other two. The electron-electron and the spin-orbit interaction are taken into account as a perturbation. This applies to 3d TM ions and 4f-5d inter-configurational transitions in RE ions.

2.3.3 The configurational coordinate diagram

So far, we have considered that the optical center A is embedded in a static lattice. However, in a real crystal, the environment of A is not static but dynamic. In order to understand the effect of the crystalline vibrations on the optical spectra, we must consider that the optically active ion A is coupled to the vibrating lattice [18]. The configurational coordinate model (Fig. 2.1) represents the energy curves in the ground and excited electronic states as a function of an effective normal mode coordinate. In the simplest case, this model which can account for such a type coupling, is based on several approximations; the Franck-Condon approximation, the harmonic approximation and the fact that only one vibration mode is considered [20].

$A = -KQ_0$ is the electron-lattice coupling constant, where K is the force constant, considered equal for the ground and excited states for simplicity, and Q_0 is the minimum of the excited state parabola. The sign of A determine whether the equilibrium distance is longer in the excited state or in the ground state, and it can be obtained from the pressure dependence of the absorption or emission spectra [21]. The shift between the

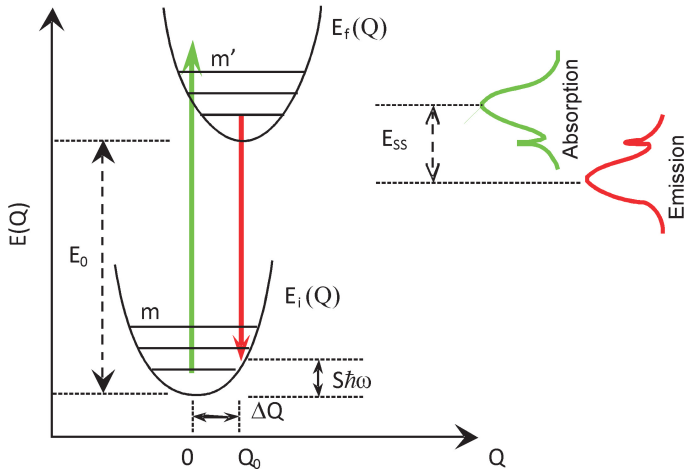

Figure 2.1: Single configurational coordinate diagram for the AB_6 center.

ground and excited states configurational curves is larger for bigger values of A. This shift which causes a displacement between emission and absorption maxima, is usually quantified by the Huang-Rhys parameter, S, defined as:

$$S = \frac{A^2}{2K\hbar\omega} = \frac{KQ_0^2}{2\hbar\omega} \tag{2.3}$$

S is a measure of the linear coupling between the electronic excited state and the vibrational mode, and it is related with the different equilibrium geometry between ground and excited states, with $S \ll 1$ for *weak coupling*, S between 1 and 4 for *medium coupling* and $S > 4$ for *strong coupling*. The energy difference between the maximum of the absorption and emission bands, E_{SS}, is called Stokes shift:

$$E_{SS} = 2S\hbar\omega \tag{2.4}$$

Then, from the experimental Stokes shift, the Huang-Rhys parameter, and therefore the distortion of the excited state with respect to the fundamental one, can be obtained. The stronger the linear coupling is, the larger the bandwith, the Huang-Rhys parameter and the Stokes shift are. f-f transitions in RE^{3+} ions show *weak coupling* with the lattice due to the mentioned shield of the 4f electrons, hence, the configurational energy curves are one above the other, and optical spectra consist of fine lines due to pure electronic transitions with small Stokes shift. On the contrary, d-d transitions in TM ions may also

show *strong coupling* giving rise to broad bands in their spectra.

2.3.4 Light absorption and emission processes

Determining the energy levels of an optically active center is important because optical spectra result from transitions among these energy levels. Different processes can take place such as absorption, due to transitions from lower energy levels to higher energy levels, and emission, in which the final state is lower in energy than the initial one. Considering a two-level system consisting of an initial state $|i>$ and a final state $|f>$ separated by an energy $E_f - E_i = \hbar\omega_{fi}$, the probability of inducing an optical transition from the state $|i>$ to the state $|f>$ upon the absorption of a photon is given by the Fermi's Golden Rule [20]:

$$W_{i\to f} = \frac{2\pi}{\hbar^2}|<i|H_{int}|f>|^2\rho_k(\omega_{fi}) \tag{2.5}$$

where H_{int} is the radiation-matter interaction Hamiltonian and $\rho_k(\omega_{fi})$ is the density of radiation field modes per unit angular velocity. The parity and spin selection rules governing a transition are determined by the matrix element $<i|H_{int}|f>$.

Relaxation from excited states can take place by both radiative and non-radiative processes. Purely radiative $|f>\to|i>$ stimulated emission presents the same transition probability as the inverse absorption process, $W_{f\to i} = W_{i\to f}$ [22]. When spontaneous emission is the radiative desexcitation channel between $|f>$ and $|i>$ states, the transition probability is given by the Einstein coefficient, $W^{sp}_{f\to i} = A_{fi}$. The rate at which the population of the $|f>$ state, N_f, decays by spontaneous emission in the absence of non-radiative processes is given by:

$$\begin{aligned} \frac{dN_f}{dt} &= -N_f A_{fi} \\ N_f(t) &= N_f(0)\exp\left(-\frac{t}{\tau_{rad}}\right) \end{aligned} \tag{2.6}$$

where τ_{rad} is the radiative lifetime of the spontaneous emission, $\tau_{rad} = \frac{1}{A_{fi}}$.

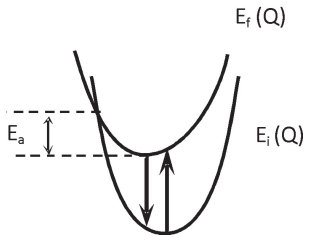

Figure 2.2: Classical interpretation of the activation energy, E_a, in non-radiative transitions.

2.3.5 Non-radiative transitions

Contrary to RE ions, in which luminescence is a quite common phenomenon even from multiple excited states, non-radiative relaxation processes usually dominate the radiative ones in TM systems. A distinction is usually made between non-radiative processes within a given complex; multiphonon relaxation, and those involving more than one optically active center; energy transfer processes [18], [22].

- *Multiphonon relaxation*: In these processes, the electronic excitation is totally or partially transformed into vibrational energy within a fempto-picoseconds timescale. Multiphonon relaxation usually occurs down to the lowest energy excited state, therefore, if luminescence exists, it takes place from this state. This is known as Kasha's rule, and RE compounds are exceptions to this rule. The configurational coordinate model (Fig. 2.2) provides a qualitative explanation to describe the temperature dependence of multiphonon relaxation from an excited state $|f>$ to some lower state $|i>$ in TM systems. According to a model proposed by Mott, the non-radiative desexcitation probability is associated to an activation energy, E_a, and is given by [23]:

$$W_{nr\,f\to i} = A \exp\left(-\frac{E_a}{kT}\right) \tag{2.7}$$

  where E_a is the energy difference between the minimum of the excited state $\mathrm{E}_f(\mathrm{Q})$ parabola and the $\mathrm{E}_i(\mathrm{Q})$ - $\mathrm{E}_f(\mathrm{Q})$ parabolas crossing point (Fig. 2.2). However, multiphonon relaxation can also be studied quantically considering tunneling processes between $|f>$ and $|i>$ states.

  In the *weak coupling case* which is characteristic for RE^{3+} compounds, the transition

rate between $|f>$ and $|i>$ states through multiphonon relaxation can be expressed as:

$$W_{nr\ f\to i}(T=0K) \propto \exp(-\beta p) = \frac{1}{\tau_{nr}} \tag{2.8}$$

This is the so-called energy gap's law, where p is the reduced energy gap and represents the number of phonons involved in the relaxation process [24]. For f $\rightarrow$ f transitions in RE ions, multiphonon relaxation processes are dominant for energy separation between levels involving $p \leq 6$.

- *Energy transfer*: All or part of the energy of an initially excited center is transferred to another center and then either emitted or converted into heat by multiphonon relaxation. In order to simplify the analysis of this kind of mechanisms, a single energy transfer step between two ions is considered:

$$S^* + A \to S + A^* \tag{2.9}$$

where S is the sensitizer (initially in an excited state) and A is the activator (in the ground state). The interaction between the two ions is responsible for the energy transfer. Transfer via electric dipole-dipole interaction was first described by Förster and later expanded by Dexter in order to include higher order electromagnetic and exchange interactions [25], [26]. The dependence of the energy transfer rate on the S and A separation, R, is R^{-6}, R^{-8} and R^{-10} for the electric dipole-dipole, dipole-quadrupole and quadrupole-quadrupole mechanisms, respectively. Energy transfer by exchange interaction requires very short S-A distances, falling off exponentially with R.

  In lanthanide systems, in which there are often several metastable excited states, cross-relaxation (CR) and UC processes are very common. In the CR mechanism, part of the high energy excitation of one ion is transferred to the partner which is typically in the ground state. One of the UC process, as we will see in Section 2.5, is exactly the reverse.

The temporal evolution of the luminescence from an excited state shows an exponential behavior in the absence of energy transfer processes, $I(t) = I_0 \exp(\frac{-t}{\tau_{total}})$, where, in

general, the total lifetime is due to contributions of both radiative and non-radiative processes, $\frac{1}{\tau_{total}} = \frac{1}{\tau_{rad}} + \frac{1}{\tau_{nr}}$. The rate equations model is extremely useful in order to describe the dynamics when energy transfer processes are involved; the temporal dependence of the S and A ions population is studied according to a system of coupled differential equations. This model has been applied in this work, considering an homogeneous impurity distribution and an average transfer rate, for the fitting of the temporal evolution of the UC luminescence in order to understand the different UC mechanisms dynamics.

2.3.6 Dimers

When two ions are close enough, they may interact strongly, lose their individual identities, and become a dimer. As a consequence, the dimer spectroscopic properties are different from those of the isolated ions. In both exchange (direct overlap of two ions orbitals) and superexchange (ions coupled through non-magnetic intermediaries) pathways, the intensity of the interaction strongly depends on the distance between the ions in the dimer, the geometry, and the electronic configuration of the ions. The so-called Goodenough-Kanamori rules correlate superexchange interactions with the structural properties. The sign and magnitude of the resulting kinetic superexchange can be predicted by consideration of the symmetry and the electron occupancy of the interacting orbitals on neighboring ions, in particular, superexchange coupling is very sensitive to the bond angle [27], [28], [29].

2.4 Raman Spectroscopy

The Raman effect is a light scattering phenomenon by which part of the incident photons frequency is used to excite vibrational modes of a molecule or solid. Most of the scattered photons emerge at the same frequency as the incident ones, ω_0, this is elastic or Rayleigh scattering. On the contrary, inelastic or Raman scattering is a much less probable event and takes place at new modified frequencies, $\omega_0 \pm \omega_k$, where ω_k are the frequencies of the Raman active vibrational modes [22]. Radiation scattered with a frequency lower than that of the incident light, $\omega_0 - \omega_k$, or Stokes scattering, is more intense than the one at higher frequency, $\omega_0 + \omega_k$, or anti-Stokes scattering. This light scattering with change of

frequency was first observed independently by Raman and Krishnan in liquids [30], [31] and Mandelstam in quartz [32] in 1928.

In a typical Raman spectrum, the measured frequencies are expressed as the difference in wavenumbers (cm^{-1}) between the incident and scattered photons, regardless of the excitation wavelength. Rayleigh scattering is a thousand times stronger than Raman scattering for strong Raman bands. The ratio of the intensities of the anti-Stokes signal to the Stokes one is related to the thermal population of the excited vibrational levels and decreases rapidly when the vibrational mode frequency, ω_k, increases. Raman spectra are strongly dependent on temperature [22]. The Raman scattering cross-section for a semiconductor is given by:

$$\frac{\mathrm{d}^2\sigma}{\mathrm{d}\Omega \mathrm{d}\omega_s} = \mathrm{vV}\frac{\omega_s^4}{\mathrm{c}^4}|\varepsilon_s \cdot \chi' \cdot \varepsilon_0|\langle UU^+\rangle_\omega \tag{2.10}$$

with

$$|\varepsilon_s \cdot \chi' \cdot \varepsilon_0| \approx \frac{\langle v|H_{int}|c\rangle\langle c|H_{ep}|c\rangle\langle c|H_{int}|v\rangle}{(\omega_g + \omega_k - \omega_0)(\omega_g - \omega_0)} \tag{2.11}$$

and

$$\langle UU^+\rangle_\omega = \frac{\hbar}{2N\omega_k}(n_k + 1)g_k(\omega) \tag{2.12}$$

where ω_s is the scattered radiation frequency, V is the total volume of the sample, v is the excited cross-section, c is the light speed, H_{int} and H_{ep} are the radiation-electron and electron-phonon interactions, v and c are the intermediate valence band (VB) and conduction band (CB) states, ω_g is the bandgap frequency, ω_k are the frequencies of the Raman active vibrational modes, and ω_0 is the frequency of the incident photons. Moreover, n_k is the phonon distribution as a function of temperature, and $g_k(\omega)$ is the phonon lorentzian line-shape factor:

$$n_k = \frac{1}{\exp\left(\frac{\hbar\omega_k}{kT}\right) - 1} \tag{2.13}$$

$$g_k(\omega) = \frac{\frac{\Gamma_k}{2\pi}}{(\omega_k - \omega)^2 + \left(\frac{\Gamma_k}{2}\right)^2} \tag{2.14}$$

The intensity of Raman scattering is defined by $I = P\alpha^2\omega_0^4$, where P is the laser power, and α is the polarizability of the electrons. The basic selection rules for Raman scattering arises from the change in polarizability. This means that, in contrast to infrared (IR) absorption, symmetric vibrations give the most intense Raman scattering. In the case of solid crystalline samples, when radiation interacts with the material, it induces vibrations through the whole lattice. Longitudinal (L) modes, along the direction of the radiation propagation, or transverse (T) modes, in a perpendicular direction, occupy a band of energies in the material. Lower energy lattice modes are called acoustic modes and labelled LA and TA while the higher energy type are called optic modes, LO and TO [33].

2.5 Upconversion

In UC processes, the emission of a high energy photon, usually in the visible, takes place upon the absorption of two or more lower energy photons, in the IR region. These kind of processes allow the conversion of the incident radiation in high energy light. UC phenomena was discovered independently by Auzel [34], [35] and Ovsyankin and Feofilov [36] in 1966. Opposite to second-harmonic generation, UC processes rely on the presence of real metastable excited states; one intermediate state which acts as a reservoir of the incident radiation, and at least one higher energy excited state from which emission occurs. The most relevant UC mechanisms are summarized in Fig. 2.3; the majority of them involve some combination of absorption and non-radiative energy transfer steps.

Fig. 2.3(a) shows the ground-state absorption/excited-state absorption (GSA/ESA) mechanism. In the GSA process the active ion is excited to an intermediate level, and it is then promoted to an upper emitting state by ESA of a second photon. This process is a single chromophore process and exhibits an immediate decay of the UC luminescence after the excitation pulse, because both GSA and ESA steps occur during the laser pulse. The efficiency strongly depends on the oscillator strength of both GSA and ESA processes, as well as on the resonance of the involved transitions with the excitation energy.

Fig. 2.3(b) describes the energy transfer upconversion (GSA/ETU) process. In this case, two ions excited by GSA to the intermediate level interact non-radiatively in order

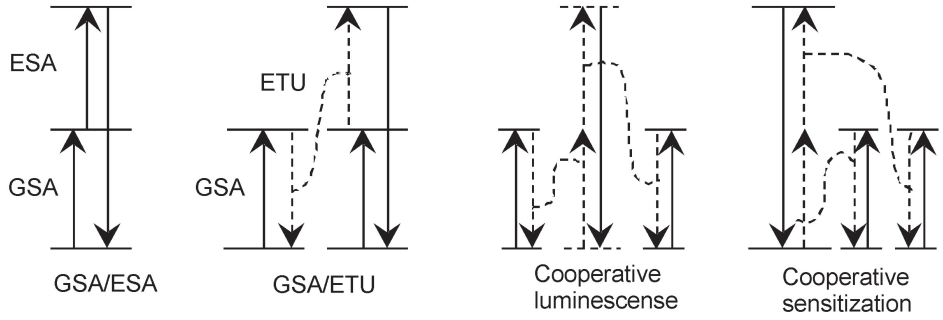

Figure 2.3: Schematic representation of the most important UC mechanisms: GSA/ESA (a), GSA/ETU (b), cooperative luminescence (c), and cooperative sensitization (d).

to generate one ion in the upper state and the other in the ground state. Since it is a non-radiative process, ETU can proceed after the pulse, and this is identified as a rise in the UC luminescence temporal evolution after a short laser pulse excitation. As we have seen in Section 2.3.5, the efficiency of the ETU mechanism depends on the distance between the two involved ions. Hence, ETU processes are very sensitive to active ions concentration.

Fig. 2.3(c) shows the cooperative luminescence. In this case, the involved ions have no metastable state to emit visible light. However, the simultaneous emission of two IR photons in two interacting ions give rise to an emitting visible photon of double energy. This is a very common process in Yb^{3+}-doped systems [37], [38], [39].

Fig. 2.3(d) describes the cooperative sensitization mechanism in which two excited sensitizer ions simultaneously transfer their excitation energy to the activator ion. This ion has no energy level resonant with the excited state of the sensitizer but it presents an excited state with twice the excitation energy from which emission takes place after non-radiative energy transfer. Its temporal behavior is expected to be similar to the GSA/ETU because it also involves an energy transfer step.

It is well known that the number of photons involved in an UC luminescence process is indicated by the slope of the luminescence intensity versus the power excitation in a double-logarithmic representation, $I \propto P^n$. This is only true, however, in the low pump power regime. Under high power excitation, the power dependence varies with the UC mechanism nature [40], [41]. Hence, both GSA/ESA and GSA/ETU shows a quadratic

power dependence under low power excitation conditions, and linear dependence at high power. The efficiency of the different UC processes depends on the number of involved optically active centers. Cooperative transitions involving three ions are about 3-4 orders of magnitude weaker than transitions between one or two ions states [42].

2.6 Rare-earth ions

Lanthanides or RE elements are those situated in the sixth period of the periodic table after the lanthanum, from cerium with the outer configuration $5s^2 5p^6 4f^1 5d^1 6s^2$, to ytterbium with configuration $5s^2 5p^6 4f^{14} 6s^2$ [20], [18]. These atoms are usually incorporated in crystals as divalent or trivalent cations. In RE^{3+} ions, 5d, 6s and some 4f electrons are removed; hence, trivalent ions deal with transitions between sub-levels of the $4f^n$ electronic configuration covering an energy range from NIR to deep UV [43]. The optically active 4f electrons are shielded by the 5s and 5p outer electrons. Because of this shielding effect, the valence electrons are weakly affected by the ligand ions in crystals. This situation corresponds to the *weak crystal field* case (see Section 2.3.2). The effect of the crystal field is to produce a slight shift in the energy of the $^{2S+1}L_J$ RE^{3+} states and to cause additional splitting. This implies that the main features of RE^{3+} ions spectra are similar comparing isolated ions to different hosts. On the contrary, RE^{2+} ions interact with the crystalline environment due to the presence of 5d electrons, and show f $\leftrightarrow$ d intraconfigurational transitions, strongly dependent on the host crystal symmetry. These f $\leftrightarrow$ d transitions are also observed in some RE^{3+} ions.

The interpretation of the RE^{3+} ions optical spectra is based on the so-called *Dieke diagram* (Fig. 2.4). Dieke *et al.* determined the energy of the $^{2S+1}L_J$ states for the RE^{3+} ions in $LaCl_3$ up to 40000 cm^{-1} [44]. Wegh *et al.* extended the *Dieke diagram* from 40000 to about 70000 cm^{-1} for various lanthanide ions [43]. The width of each state indicates the magnitude of the crystal-field splitting, it is smaller than 1000 cm^{-1} in all cases. This value is in general lower than the spin-orbit splitting. The free ion energy levels are given by the center of gravity of each multiplet. The same spin-orbit terms in an inverse energy order for the $4f^n$ and $4f^{14-n}$ configurations is evidenced in *Dieke diagram*. Besides, a comparison of the energy levels of Ce^{3+} and Yb^{3+} shows clearly the spin-orbit parameter

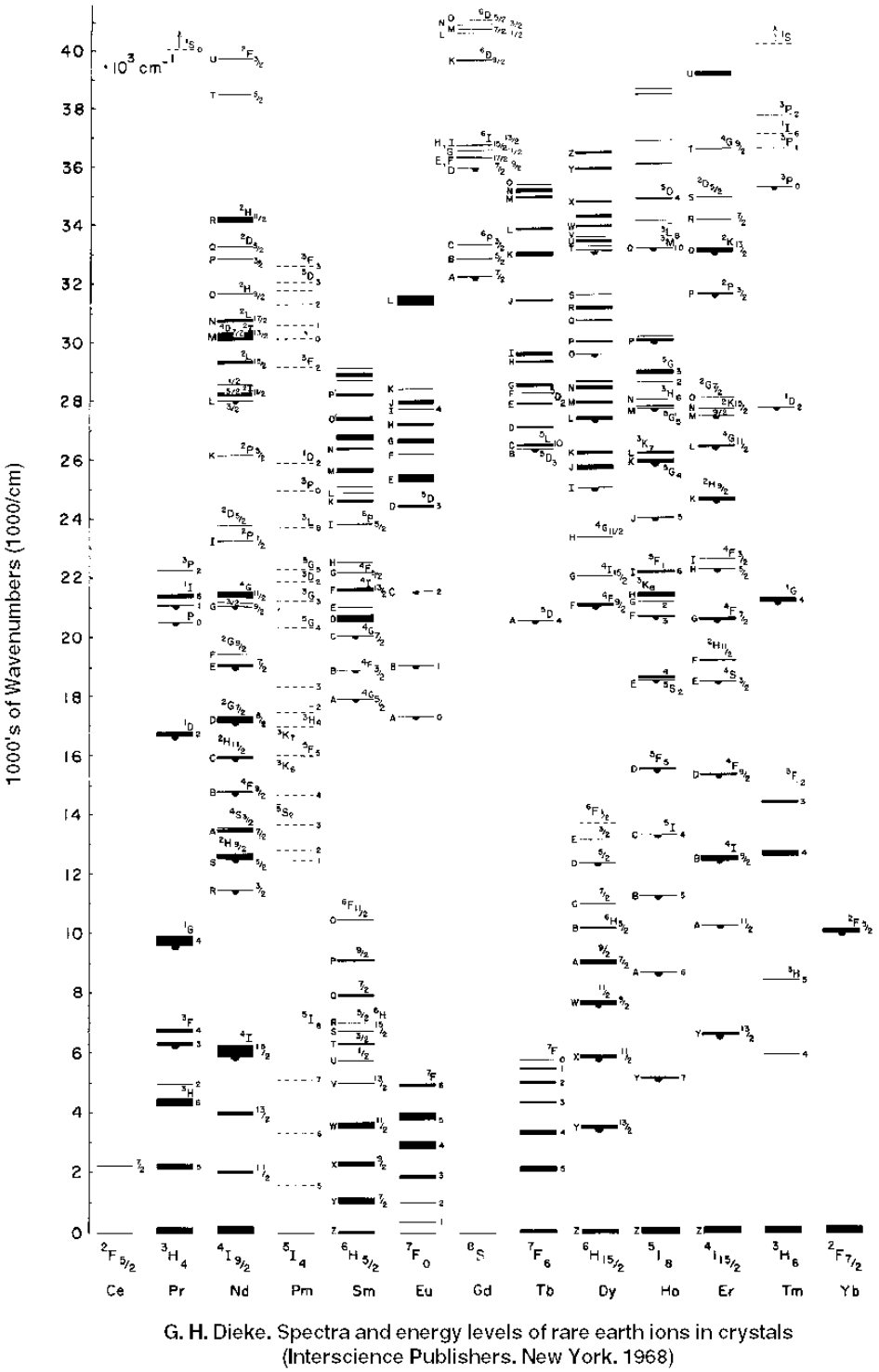

Figure 2.4: Dieke diagram of RE^{3+} ions in $LaCl_3$ [44]. Semicircles indicate the emitting levels.

increase for larger atomic number.

Since electron-phonon coupling effects are weak, optical transitions between $4f^n$ states in RE^{3+} are characterized by sharp lines. These transitions occur between states of the same parity and then they are expected to occur by a magnetic dipole process. However, a mixing of $4f^n$ states with opposite-parity states of the $4f^{n-1}$-5d configuration can take place by coupling with odd vibrational modes, allowing a forced electric dipole component to the transition. Spin is not a good quantum number to consider in f-f transitions because of the spin-orbit coupling. Some general selection rules for electric dipole transitions between RE^{3+} $4f^n$ states obtained from the Judd-Ofelt theory are $|\Delta J| \leq 6$ with $J = 0 \leftrightarrow J' = 0$ forbidden, and $J = 0 \leftrightarrow$ odd J' much weaker than $J = 0 \leftrightarrow$ even J' [20]. Interconfigurational $4f^n \leftrightarrow 4f^{n-1}5d$ transitions are parity allowed and usually appear in the UV region for RE^{3+} ions. Their energy strongly depends on the local environment because 5d levels are not so efficiently screened.

2.7 Transition metal ions

TM ions (iron group) are formed from the elements situated in the fourth period of the periodic table in which the 3d shell is being filled. In ionic solids, such elements lose the outer 4s electrons and some 3d electrons, and their electronic configurations are $1s^22s^22p^63s^23p^63d^n$, where $n < 10$ [20]. Since 3d electrons, responsible for the optical transitions, interact strongly with electric fields of nearby ions, the crystal-field effects are, in general, more important than for RE^{3+} ions. Besides, TM ions show strong electron-lattice coupling; as a result, the spectra can present both broad ($S > 0$) and sharp ($S \sim 0.1$) bands [18]. According to the *strong crystal field* scheme, and taking into account that the electron-electron and crystal-field interactions dominate over the spin-orbit term, the electronic levels splitting of the TM ion can be obtained according to each complex symmetry [20]. In an octahedral crystal field, the five d levels are split into a triply-degenerate level t_{2g} and a doubly-degenerate level e_g; the strength of the crystal field responsible for this splitting, Δ, is called 10Dq. The energy of the transitions observed experimentally in the TM spectra can be described by using Δ=10Dq and the so-called Racah parameters B and C [45].

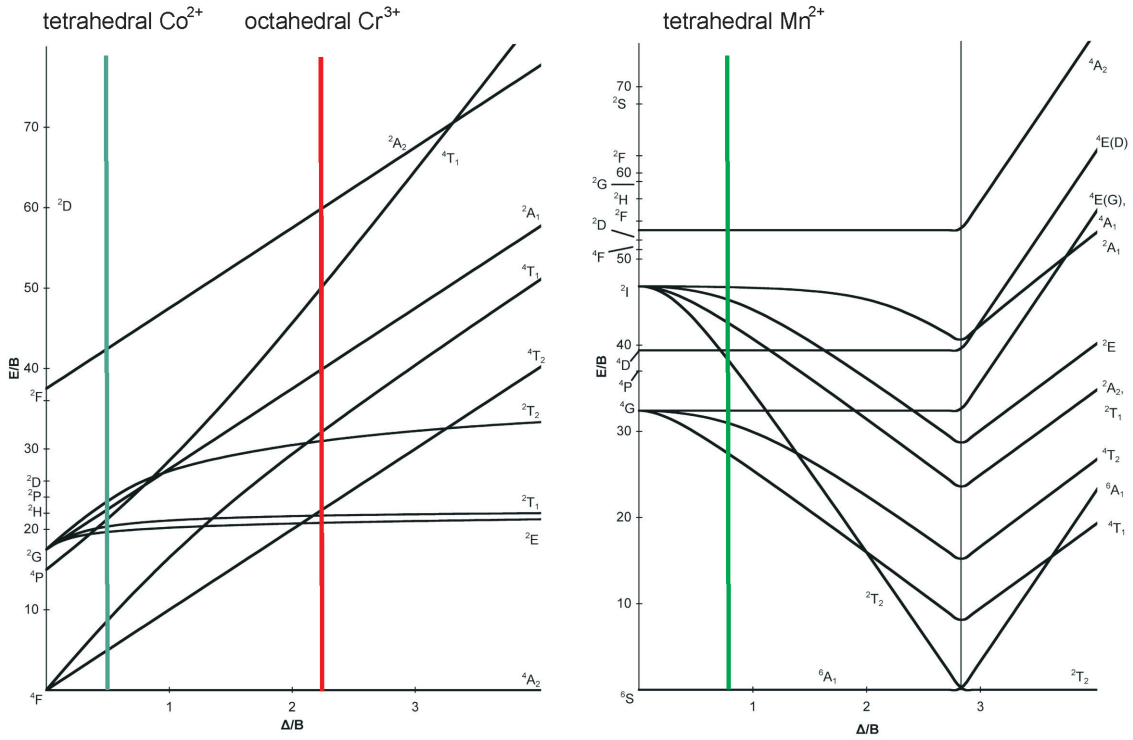

Figure 2.5: Tanabe-Sugano diagram for a d^3 ion in an octahedral crystal field or a d^7 ion in a tetrahedral crystal field (left), and Tanabe-Sugano diagram for a d^5 ion (right). The vertical lines indicate the crystal field strength for Co^{2+}, Cr^{3+} and Mn^{2+} ions, in the lattices studied in this work; ZnO, $Gd_3Ga_5O_{12}$ and $LaMgAl_{11}O_{19}$, respectively.

Sugano and Tanabe calculated the energy of the states deriving from d^n ions ($2< n <8$) as a function of the octahedral crystal field. These calculations are represented in the *Tanabe-Sugano diagrams* which show the energy of the states in units of B (E/B) compared to the ground state energy, as a function of the ratio between the crystal-field strength and the interelectronic interaction, measured in units of Δ/B, for a given C/B ratio [46]. The energy level scheme of a $3d^{10-n}$ ion in a tetrahedral crystal field is the same as in an octahedral crystal field but with negative 10Dq, hence, it has the same pattern as the splitting of a $3d^n$ system in an octahedral crystal field. The relationship between the crystal-field strenghts is given by 10Dq(octahedral)$= -\frac{9}{4}$ 10Dq(tetrahedral). Figure 2.5 shows the *Tanabe-Sugano diagrams* for d^3 and d^5 systems in an octahedral crystal field. These diagrams are appropriate to describe the TM ions that have been studied in this work: Cr^{3+} ($3d^3$ system) in an octahedral crystal field and Co^{2+} ($3d^7$ system) in a tetrahedral crystal field (Fig. 2.5(a)), and Mn^{2+} ($3d^5$ system) in a tetrahedral crystal

field (Fig. 2.5(b)). *Tanabe-Sugano diagrams* allow to predict if an optical band of a TM ion is narrow or broad from the slope of the involved states. In general, the magnitude of the slope is proportional to the electron-lattice coupling constant. Therefore, the states with energies independent of the crystal field give rise to narrow bands while broad bands are associated with transitions involving large slope energy levels. Despite the fact that non-radiative processes are more important in TM than in RE systems, UC luminescence processes have also been observed in different TM ions such as Pb^{+}, Ti^{2+}, Mn^{2+}, Ni^{2+} or Cr^{3+} [47], [48], [49], [50].

2.8 Semiconductor nanostructures

The bandgap of a semiconductor is defined as the energy difference between the highest energy VB states and the lowest energy CB states. If an electron is excited from the VB to the CB leaving a hole in the VB, the electron-hole (e-h) pair may form a bound state through Coulomb interactions. This bound state (the so-called Wannier-Mott or free exciton) has an energy slightly lower than the bandgap energy. The Bohr radius of the exciton, a_B, is given by the following equation:

$$a_B = \frac{4\pi\varepsilon_0\varepsilon_\infty\hbar^2}{m_0 e^2}\frac{1}{\mu^*} = a_0\varepsilon_\infty\frac{1}{\mu^*} \tag{2.15}$$

where ε_0 is the vacuum dielectric constant, ε_∞ is the high frequency relative dielectric constant of the medium, m_0 is the mass of the free electron, μ^*, with $\frac{1}{\mu^*} = \frac{1}{m_e^*} + \frac{1}{m_h^*}$, is the effective reduced e-h mass (m_e^* and m_h^* are the effective electron and hole masses), and a_0 is the Bohr radius of a hydrogen atom (0.529 Å). Since the effective masses are significantly smaller than m_0, and ε_∞ is much larger than 1, the resulting values for a_B are much larger than a_0, in the range 1-10 nm for the common semiconductors. The Bohr radius of the exciton is 2.6 nm for bulk CdS in the ZB structure [51] and 0.9 nm for bulk W-ZnO [52]. Semiconductor nanoparticles exhibit quantum size or quantum confinement effects when the dimensions of the system approaches the Bohr radius of the exciton, as a result of spatial confinement of the electrons and holes in the nanoparticles; in these cases, they are also called QDs [53], [54]. Two manifestations of these quantum size effects are

the increase in the bandgap with decreasing particle size, and the transition from energy bands to discrete energy levels. The chemical bonds contraction at the surface due to coordination deficiency and the rise of the surface-to-volume ratio have been shown to be responsible for these changes at the nanoscale [55].

Different approaches have been proposed to explain the bandgap expansion of semiconductor nanocrystals [55]. The widely accepted model was initially proposed by Efros [56] and further extended by Brus [53], [57] to include the term of Coulomb interaction of an e-h pair. The confinement effect on the bandgap, E_g, is then expressed as a function of the semiconductor nanoparticle radius, R:

$$E_g(R) = E_g + \frac{\pi^2\hbar^2}{2m_0R^2}\frac{1}{\mu^*} - \frac{1.8e^2}{4\pi\varepsilon_0\varepsilon_\infty R} \tag{2.16}$$

where the first term, E_g, represents the bandgap of the bulk semiconductor, the second term represents the spatial confinement of electrons in the CB and holes in the VB by the potential barrier of the surface or a mono-potential well of the quantum box and has a $1/R^2$ dependence, and the third term represents the Coulomb energy with a $1/R$ dependence. Generally, the second term is more important than the third one, leading to an increase in the QDs energy bandgap when reducing the particle size.

2.9 Interband absorption in semiconductors

2.9.1 Introduction

Semiconductors absorption spectra in the visible region are due to interband transitions, in which an electron is excited from the VB to the CB. A continuous absorption spectrum starting from the low energy threshold at the energy bandgap, E_g, is observed for bulk semiconductors. A step-like behavior is expected for quantum wells while a series of delta functions is predicted for QDs [17]. Although the joint density of states changes when the QDs size is reduced, the only size effect that has been considered in this work is the blue-shift of the absorption edge with decreasing particle size. Therefore, the equations describing interband transitions in bulk semiconductors have been used, and are shown in the next two sections. The interband absorption rate depends on the band

structure of the solid. Considering the relative positions of the CB minimum and the VB maximum in the Brillouin zone, the bandgap may be direct or indirect. Conservation of momentum implies that absorption processes are represented by vertical lines on E-k diagrams. Hence, if the bandgap is indirect, the transition must involve a phonon to satisfy momentum conservation [17].

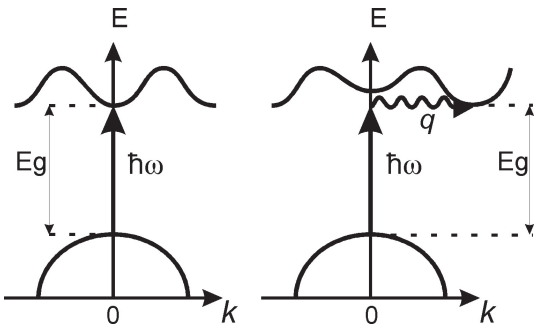

Figure 2.6: Interband transitions in semiconductors. Direct bandgap (a) and indirect bandgap (b).

2.9.2 Band edge absorption in direct gap semiconductors

In a direct gap semiconductor, both the VB maximum and the CB minimum occur at the same value of $\boldsymbol{k}$ (see Fig. 2.6(a)). Assuming a simplified parabolic form for the VB and CB, the conservation of energy during a transition requires that:

$$\hbar\omega = E_g + \frac{\hbar^2 k^2}{2\mu} \tag{2.17}$$

where μ is the reduced e-h mass. The joint e-h density of states, $g(\hbar\omega)$, is then given by:

$$\begin{aligned} g(\hbar\omega) &= 0 \quad \text{For } \hbar\omega < E_g \\ g(\hbar\omega) &= \frac{1}{2\pi^2}\left(\frac{2\mu}{\hbar^2}\right)^{3/2}(\hbar\omega - E_g)^{1/2} \quad \text{For } \hbar\omega \geq E_g \end{aligned} \tag{2.18}$$

Fermi's Golden Rule tells us that the absorption rate for a dipole-allowed interband transition is proportional to the joint density of states. Hence, the following behavior is expected for the frequency dependence of the absorption coefficient, $\alpha(\hbar\omega)$ [17]:

$$\begin{aligned} \alpha(\hbar\omega) &= 0 \quad \text{For } \hbar\omega < E_g \\ \alpha(\hbar\omega) &\propto (\hbar\omega - E_g)^{1/2} \quad \text{For } \hbar\omega \geq E_g \end{aligned} \tag{2.19}$$

According to eq. (2.19), a straight line behavior is obtained plotting α^2 against the photon energy, $\hbar\omega$, in the spectral region close to the bandgap. The bandgap is the point at which the absorption goes to zero.

2.9.3 Band edge absorption in indirect gap semiconductors

Indirect gap materials have their CB minimum away from the Brillouin zone center, as shown schematically in fig. 2.6(b). A photon can excite an electron from the VB to the CB involving a phonon to conserve momentum, $\boldsymbol{k}$. Conservation of energy and momentum requires that:

$$\hbar\omega = E_{CV} \pm \hbar\Omega \tag{2.20}$$

$$\boldsymbol{k_V} - \boldsymbol{k_C} = \pm\boldsymbol{Q} \tag{2.21}$$

where E_{CV} is the difference in energy between VB and CB, $\hbar\Omega$ is the phonon energy, $\boldsymbol{k_V}$ and $\boldsymbol{k_C}$ are the respective wave vectors of the involved states in VB and CB, and $\boldsymbol{Q}$ is the phonon wave vector. The $\pm$ sign represents the phonon absorption or emission. Indirect transitions are second-order processes, the transition rate is therefore much smaller than for direct absorption. The frequency dependence of the indirect absorption coefficient in this case is given by:

$$\alpha_i(\hbar\omega) \propto (\hbar\omega - E_g \mp \hbar\Omega)^2 \tag{2.22}$$

If $\alpha^{1/2}$ is plotted against $\hbar\omega$, the indirect gap semiconductor data fits well to a straight line. The experimental data also shows a tail caused by higher frequency phonons or multiphonon absorption.

It must be pointed out that since the frequency dependence is different for direct and indirect gap semiconductors, it provides a very convenient way to determine the nature of the bandgap.

2.10 Structural phase transitions. Equations of state

The crystalline structure of a solid may undergo modifications when pressure or temperature conditions are changed. The different phases of a given material together with its $P-T$ stability points compose the phase diagram of the material. From a thermodynamic point of view, a given phase is stable when the Gibbs free energy is minimum. First-order phase transitions exhibit a discontinuity in the first derivative of the Gibbs free energy. A diminution of the volume or the entropy is experimentally observed at the transition point. Transitions showing hysteresis in both pressure and temperature are first-order transitions. Second-order phase transitions are continuous in the first derivative but exhibit discontinuity in a second derivative of the free energy, they take place at well-defined temperature and pressure, and they present no hysteresis [58]. It is important to point out that pressure-induced phase transitions lead to transformations to more compact structures, increasing the coordination number and involving volume reduction. Density increases and, therefore, they are usually first-order phase transitions.

The appearance of a structural phase transition may have important consequences not only in the structural characterization measurements, but also in the optical properties. The absorption or emission spectra of an optically active ion change drastically if the new phase involves modifications of the coordination number or bond distances. Besides, changes in the bandgap absorption and Raman spectra of semiconductor materials, associated to the transformation into a new crystalline structure are also very common.

An equation of state provides a relationship between two or more state variables, such as temperature, pressure or volume. For a given phase, temperature, volume, and pressure are not independent quantities; they are connected by a relationship of the general form $f(P,V,T) = 0$. For first-order phase transitions, each structural phase in the $P-T$ diagram has a characteristic equation of state.

Considering an isothermal relation between P and V, the simplest reasonable model for an equation of state would be with a constant bulk modulus, $B_0 = -V\left(\frac{\partial P}{\partial V}\right)_T$. A more sophisticated equation of state was derived by Murnaghan assuming that isothermal B is a linear function of P, $B = B_0 + B_0' \cdot P$. The bulk modulus pressure derivative, $B' = \left(\frac{\partial B}{\partial P}\right)_T$,

is considered constant, $B' = B'_0$, and therefore [59]:

$$V(P) = V_0 \left(1 + \frac{B'_0}{B_0} P\right)^{-1/B'_0} \tag{2.23}$$

V_0 being the equilibrium volume, $V(P = 0)$. This equation is appropriate for compressions lower than 15%, however, for higher compressions more elaborated equations of state are needed, such as Birch-Murnaghan equation [60] or Rose-Vinet equation [61].

Bibliography

[1] G.L. Hornyak, J. Dutta, H.F. Tibbals, and A.K. Rao, editors. *Introduction to Nanoscience*. CRC Press, Taylor and Francis group, Florida, 2008.

[2] A. Trave, F. Buda, and A. Fasolino. Band-Gap Engineering by III-V Infill in Sodalite. *Phys. Rev. Lett.*, **77**: 5405–5408, 1996.

[3] J.R. Agger, M.W. Anderson, M.E. Pemble, O. Terasaki, and Y. Nozue. Growth of Quantum-Confined Indium Phosphide inside MCM-41. *J. Phys. Chem. B*, **102**: 3345–3353, 1998.

[4] F. Vetrone, J.C. Boyer, J.A. Capobianco, A. Speghini, and M. Bettinelli. A spectroscopic investigation of trivalent lanthanide doped Y_2O_3 nanocrystals. *Nanotech.*, **15**: 75–81, 2004.

[5] C. Ricolleau, L. Audinet, M. Gandais, and T. Gacoin. Structural transformations in II-VI semiconductor nanocrystals. *Eur. Phys. J. D*, **9**: 565–570, 1999.

[6] E.L. Wolf, editor. *Nanophysics and Nanotechnology*. Wiley-VCH, Weinheim, Germany, 2004.

[7] M. Stupca, M. Alsalhi, T. Al Saud, A. Almuhanna, and M.H. Nayfeh. Enhancement of polycrystalline silicon solar cells using ultrathin films of silicon nanoparticle. *Appl. Phys. Lett.*, **91**: 063107, 2007.

[8] M. Bruchez Jr, M. Moronne, P. Gin, S. Weiss, and A.P. Alivisatos. Semiconductor Nanocrystals as Fluorescent Biological Labels. *Science*, **281**: 2013–2016, 1998.

[9] R. Elghanian, J.J. Storhoff, R.C. Mucic, R.L. Letsinger, and C.A. Mirkin. Selective Colorimetric Detection of Polynucleotides Based on the Distance-Dependent Optical Properties of Gold Nanoparticles. *Science*, **277**: 1078–1081, 1997.

[10] W.C.W. Chan and S. Nie. Quantum Dot Bioconjugates for Ultrasensitive Nonisotopic Detection. *Science*, **281**: 2016–2018, 1998.

[11] M. Nyk, R. Kumar, T.Y. Ohulchanskyy, E.J. Bergey, and P.N. Prasad. High Contrast in Vitro and in Vivo Photoluminescence Bioimaging Using Near Infrared to Near Infrared Up-Conversion in Tm^{3+} and Yb^{3+} Doped Fluoride Nanophosphors. *Nano Lett.*, **8**: 3834–3838, 2008.

[12] F. Vetrone and J.A. Capobianco. Lanthanide-doped fluoride nanoparticles: luminescence, upconversion, and biological applications. *Int. J. Nanotech.*, **5**: 1306–1339, 2008.

[13] C. Vancaeyzeele, O. Ornatsky, V. Baranov, L. Shen, A. Abdelrahman, and M.A. Winnik. Lanthanide-Containing Polymer Nanoparticles for Biological Tagging Applications: Nonspecific Endocytosis and Cell Adhesion. *J. Am. Chem. Soc.*, **129**: 13653–13660, 2007.

[14] P.V. Kamat. Meeting the Clean Energy Demand: Nanostructure Architectures for Solar Energy Conversion. *J. Phys. Chem. C*, **111**: 2834–2860, 2007.

[15] A. Shalav, B.S. Richards, and T. Trupke. Application of $NaYF_4$: Er^{3+} up-converting phosphors for enhanced near-infrared silicon solar cell response. *Appl. Phys. Lett.*, **86**: 013505, 2005.

[16] L. Aarts, B.M. van der Ende, and A. Meijerink. Downconversion for solar cells in $NaYF_4$: Er, Yb. *J. Appl. Phys.*, **106**: 023522, 2009.

[17] M. Fox, editor. *Optical Properties of Solids*. Oxford University Press, Oxford, 2001.

[18] J. García Solé, L.E. Bausá, and D. Jaque, editors. *An Introduction to the Optical Spectroscopy of Inorganic Solids*. John Wiley and Sons Ltd, England, 2005.

[19] J.S. Griffith, editor. *The Theory of Transition-Metal Ions*. Cambridge University Press, London, 1971.

[20] B. Henderson and G.F. Imbusch, editors. *Optical Spectroscopy of Inorganic Solids*. Clarendon Press, Oxford, 1989.

[21] R. Valiente, F. Rodríguez, J. González, H.U. Güdel, R. Martín-Rodríguez, L. Nataf, M.N. Sanz-Ortiz, and K. Krämer. High pressure optical spectroscopy of Ce^{3+}-doped $Cs_2NaLuCl_6$. *Chem. Phys. Lett.*, **481**: 149–151, 2009.

[22] E.I. Solomon and A.B.P. Lever, editors. *Inorganic Electronic Structure and Spectroscopy*, volume I. John Wiley and Sons, New York, 1999.

[23] N.F. Mott. *Proc. Roy. Soc. (London)*, **A 167**: 384, 1938.

[24] J.M.F. van Dijk and M.F.H. Schuurmans. On the nonradiative and radiative decay rates and a modified exponential energy gap law for 4f−4f transitions in rare-earth ions. *J. Chem. Phys.*, **78**: 5317–5323, 1983.

[25] T. Förster. *Ann. der Physik*, **2**: 55, 1948.

[26] D.L. Dexter. *J. Chem. Phys.*, **21**: 836, 1953.

[27] J.B. Goodenough, editor. *Magnetism and the Chemical Bond*. Interscience-Wiley, New York, 1963.

[28] J. Kanamori. *J. Phys. Chem. Solids*, **10**: 87, 1959.

[29] H. Weihe and H.U. Güdel. Quantitative Interpretation of the Goodenough-Kanamori Rules: A Critical Analysis. *Inorg. Chem.*, **36**: 3632–3639, 1997.

[30] C.V. Raman and K.S. Krishnan. A New Type of Secondary Radiation. *Nature*, **121**: 501–502, 1928.

[31] C.V. Raman. A Change of Wave-length in Light Scattering. *Nature*, **121**: 619–619, 1928.

[32] G.S. Landsberg and L.J. Mandeltsam. Eine neue Erscheinung bei der Lichtzerstreuung in Krystallen. *Naturwissenschaften*, **16**: 557–558, 1928.

[33] W.E. Smith and G. Dent, editors. *Modern Raman Spectroscopy - A Practical Approach*. John Wiley and Sons, England, 2005.

[34] F. Auzel. *Acad. Sci.*, **262**: 1016, 1966.

[35] F. Auzel. *Acad. Sci.*, **263 B**: 765, 1966.

[36] V.V. Ovsyankin and P.P. Feofilov. *Jetp. Lett.*, **3**: 322, 1966.

[37] E. Nakazawa and S. Shionoya. Cooperative Luminescence in $YbPO_4$. *Phys. Rev. Lett.*, **25**: 1710–1712, 1970.

[38] P. Goldner, F. Pellé, D. Meichenin, and F. Auzel. Cooperative luminescence in ytterbium-doped $CsCdBr_3$. *J. Lumin.*, **71**: 137–150, 1997.

[39] M.P. Hehlen and H.U. Güdel. Optical spectroscopy of the dimer system $Cs_3Yb_2Br_9$. *J. Chem. Phys.*, **98**: 1768–1775, 1993.

[40] M. Pollnau, D.R. Gamelin, S.R. Lüthi, H.U. Güdel, and M.P. Hehlen. Power dependence of upconversion luminescence in lanthanide and transition-metal-ion systems. *Phys. Rev. B*, **61**: 3337–3346, 2000.

[41] J.F. Suyver, A. Aebischer, S. García-Revilla, P. Gerner, and H.U. Güdel. Anomalous power dependence of sensitized upconversion luminescence. *Phys. Rev. B*, **71**: 125123, 2005.

[42] F. Auzel. Upconversion and Anti-Stokes Processes with f and d ions in Solids. *Chem. Rev.*, **104**: 139–173, 2004.

[43] R.T. Wegh, A. Meijerink, R.J. Lamminmäki, and J. Hölsä. Extending Dieke's diagram. *J. Lumin.*, **87-89**: 1002–1004, 2000.

[44] G.H. Dieke, editor. *Spectra and Energy Levels of Rare Earth Ions*. Wiley Interscience, New York, 1968.

[45] S. Sugano and Y. Tanabe. *J. Phys. Soc. Jpn.*, **9**: 753, 1954.

[46] S. Sugano, Y. Tanabe, and H. Kamimura, editors. *Multiplets of transition metal ions in solids.* Academic Press, New York, 1970.

[47] J.M. Spaeth, R.H. Bartram, M. Rac, and M. Fockele. Upconversion by excited state absorption of Pb^{+}(1) centres in alkaline-earth fluorides. *J. Phys.: Condens. Matter*, **3**: 5013–5022, 1991.

[48] R. Valiente, O.S. Wenger, and H.U. Güdel. New photon upconversion processes in Yb^{3+} doped $CsMnCl_3$ and $RbMnCl_3$. *Chem. Phys. Lett.*, **320**: 639–644, 2000.

[49] S. García-Revilla, P. Gerner, H.U. Güdel, and R. Valiente. Yb^{3+}-sensitized visible Ni^{2+} photon upconversion in codoped $CsCdBr_3$ and $CsMgBr_3$. *Phys. Rev. B*, **72**: 125111, 2005.

[50] S. Heer, M. Wermuth, K. Krämer, and H.U. Güdel. Sharp ^{2}E upconversion luminescence of Cr^{3+} in $Y_3Ga_5O_{12}$ codoped with Cr^{3+} and Yb^{3+}. *Phys. Rev. B*, **65**: 125112, 2002.

[51] Y. Kayanuma. Quantum-size effects of interacting electrons and holes in semiconductor microcrystals with spherical shape. *Phys. Rev. B*, **38**: 9797–9805, 1988.

[52] V.A. Fonoberov and A.A. Balandin. Radiative lifetime of excitons in ZnO nanocrystals: The dead-layer effect. *Phys. Rev. B*, **70**: 195410, 2004.

[53] L.E. Brus. Electron-electron and electron-hole interactions in small semiconductor crystallites: The size dependence of the lowest excited electronic state. *J. Chem. Phys.*, **80**: 4403–4409, 1984.

[54] P.F. Trwoga, A.J. Kenyon, and C.W. Pitt. Modeling the contribution of quantum confinement to luminescence from silicon nanoclusters. *J. Appl. Phys.*, **83**: 3789–3794, 1998.

[55] C.Q. Sun, T.P. Chen, B.K. Tay, S. Li, H. Huang, Y..B Zhang, L.K Pan, S.P. Lau, and X.W. Sun. An extended quantum confinement theory: surface-coordination

imperfection modifies the entire band structure of a nanosolid. *J. Phys. D: Appl. Phys.*, **34**: 3470–3479, 2001.

[56] Al.L. Efros and A.L. Efros. Interband absorption of light in a semiconductor sphere. *Sov. Phys. Semicond.*, **16**: 772–775, 1982.

[57] L.E. Brus. On the development of bulk optical properties in small semiconductor crystallites. *J. Lumin.*, **31-32**: 381–384, 1984.

[58] R. Ehrenfest. *Proc. Acad. Sci. Amsterdam*, **36**: 153–157, 1933.

[59] F.D. Murnaghan. The Compressibility of Media under Extreme Pressures. *P. Natl. Acad. Sci.*, **30**: 244–247, 1944.

[60] F. Birch. Finite Elastic Strain of Cubic Crystals. *Phys. Rev.*, **71**: 809–824, 1947.

[61] P. Vinet, J. Ferrante, J.R. Smith, and J.H. Rose. A universal equation of state for solids. *J. Phys. C: Solid State Phys.*, **19**: L467–L473, 1986.